Journal of Electronic Imaging

JElectronicImaging.org

Compton scattering imaging system with two scanning configurations

Cécilia Tarpau
Mai K. Nguyen

SPIE. IS&T imaging.org

Cécilia Tarpau, Mai K. Nguyen, "Compton scattering imaging system with two scanning configurations," *J. Electron. Imaging* **29**(1), 013005 (2020), doi: 10.1117/1.JEI.29.1.013005

Compton scattering imaging system with two scanning configurations

Cécilia Tarpau[a,b,c,*] and Mai K. Nguyen[a]
[a]University of Cergy Pontoise, Equipes Traitement de l'Information et Systèmes, ENSEA, CNRS UMR 8051, Cergy Pontoise, France
[b]University of Cergy Pontoise, Laboratoire de Physique Théorique et Modélisation, CNRS UMR 8089, Cergy Pontoise, France
[c]University of Versailles Saint Quentin, Laboratoire de Mathématiques de Versailles, CNRS UMR 8100, Versailles, France

Abstract. The judicious use of Compton scattered radiation continues to be a relevant challenge for the future of tomographic imaging. In this context, a new modality of Compton scattering tomography has been recently proposed. This new system has the advantage of being fixed, with a source and detectors placed on a ring passing through the source. The objective of this paper is to explore new possibilities for this new modality: scanning both small and large objects via a double scanning configuration. In fact, when an object under study is small and can be placed inside the detector ring, its scanning will be performed by the interior configuration. Otherwise, a large object placed outside the system will be scanned by the exterior configuration. The modeling of data acquisition of these two scanning modes leads to a new Radon transform on circular arcs (CirArcRT), established for the first time. Image reconstruction requires the inversion of CirArcRT, which is obtained via geometric inversion (GI). In fact, GI allows converting the circular arcs into corresponding half-lines, and consequently, the CirArcRT into a new Radon transform on half-lines, whose inversion is established. Numerical simulations are carried out to demonstrate the feasibility of the new modality. The ability for the same system to scan both small and large objects enlarges the fields of applications for tomography from biomedical imaging to nondestructive testing in industry as well as cultural heritage objects imaging. [DOI: 10.1117/1.JEI.29.1.013005]

Keywords: Compton scattering tomography; Radon transform on circular arcs; Radon transform on half-lines; data acquisition; image reconstruction.

Paper 190813 received Sep. 19, 2019; accepted for publication Dec. 11, 2019; published online Jan. 14, 2020.

1 Introduction

The possibility to probe matter and see (invisible) hidden structures becomes a reality with various imaging techniques, especially with ionizing radiation imaging, thanks to its ability of deep penetration into matter. This explains why the latter is widely used in nuclear medicine, nondestructive evaluation in industry or security surveillance, etc.

Computed tomography (CT) falls within the conventionally used imaging techniques. CT exploits transmitted radiation, attenuated by the object under study. Data acquisition and image reconstruction with this technique are modeled, respectively, by the forward and inverse Radon transform (RT) on straight lines.[1,2] CT uses only primary (that is, not deviated) radiation for image reconstruction. As a consequence, scattered radiation is considered as noise that degrades image quality (causing blurs, loss of image contrast, false detection, etc.). The solution for CT is the use of collimators in order to eliminate as much as possible the scattered photons. This reduces drastically the acquired data (one photon over ten thousands emitted photons arrives at detector due to the presence of collimators[3]).

*Address all correspondence to Cécilia Tarpau, E-mail: cecilia.tarpau@ensea.fr

1017-9909/2020/$28.00 © 2020 SPIE and IS&T

1.1 *Emergence, Functioning Principle, and Advantages of Compton Scattering Tomography*

Over the past century, many studies prove that scattered radiation contains useful information about the structures of an object, sufficient information for image reconstruction. Moreover, in some practical cases where it is impossible to rotate the couple source–detector (one-sided massive objects like walls, for example), conventional CT cannot be used. Hence, the idea to wisely use the information from Compton scattered radiation for image reconstruction came up, with the proposition of modalities of Compton scattering tomography (CST). CST modalities allow the access to a new characteristic of the object namely the density of electrons (scattering sites in the object).

The Compton formula, is the key of the functioning principle of CST modalities, giving a bijection between energy $E(\omega)$ and scattering angle ω:

$$E(\omega) = \frac{E_0}{1 + \frac{E_0}{mc^2}[1 - \cos(\omega)]}, \tag{1}$$

where E_0 is the energy of the emitted ray and mc^2 is the energy of an electron at rest. Moreover, this one-to-one correspondence means also that scattered photons at $E(\omega)$ have their scattering sites on a circular arc. This circular arc passes through the source and the detector, subtending the angle $(\pi - \omega)$. Figure 1 shows examples of scattered photons paths for two different scattering angles ω_1 and ω_2, given a source S and a detector D. The circular arcs $\mathcal{A}(S, D, \omega_1)$ and $\mathcal{A}(S, D, \omega_2)$ are loci of the possible scattering sites, respectively, for ω_1 and ω_2. Finally, M_k and M'_k are running points (scattering sites) of these circular arcs.

Advantages of CST systems are numerous for both biomedical and industrial imaging. For the energy range of x-rays used for biomedical imaging, Compton effect is the predominant physical interaction in tissues and single scattering represents almost 80% of scattered radiation.[4] The measurement of electronic density is particularly useful for radiation therapy.[5] Consequently, CST can offer a higher contrast (compared to the classical tomographic imaging) useful for scanning small objects, tracking tumors or to observe calcification in the breast[5,6] with no additional radiation dose. Second, for industrial applications, CST systems are convenient for scanning one-sided objects[7] or objects with thin layers. Moreover, Compton scattering is the predominant attenuation effect for materials having a low atomic number (like carbon and aluminum) for the energy range of 100 to 200 keV, making the CST imaging particularly interesting for composite materials.[7] More notably, the performance of CST has been studied earthquake engineering,[8] cultural heritage objects imaging,[9,10] landmine detection,[11] and agricultural measurements.[12]

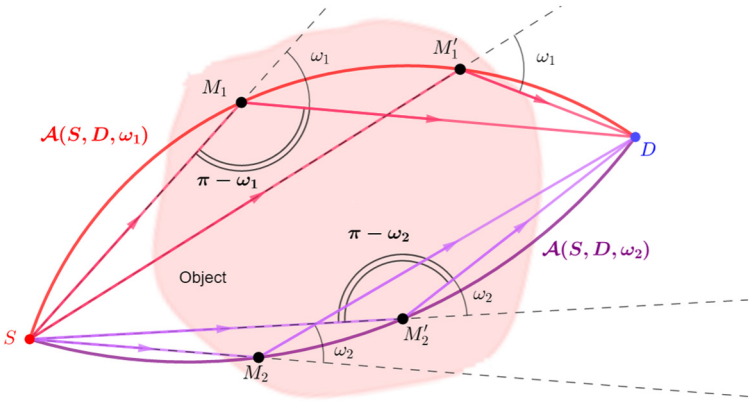

Fig. 1 Functioning principle of CST modalities.

1.2 *Challenges Raised by CST Modalities*

CST modalities lead to two different challenges: theoretical and technological. The theoretical one concerns the modeling of image formation and reconstruction. In fact, image formation with CST modalities are mathematically modeled by generalizations of the classical RT on families of circular arcs (corresponding to the locations of the scattering sites), according to the geometry of the CST system. Finally, image reconstruction requires the inversion of these new generalized RTs and this step constitutes the main theoretical challenge raised by CST. Furthermore, designing CST modalities imposes the use of multienergy range detectors having a sufficient energy resolution.

1.3 *Review on Previous CST Modalities*

In this context, some CST modalities and the associated RT have been introduced in order to answer to the theoretical challenge of CST systems. The first CST system was proposed by Norton.[13] This modality, composed of a source and a line of detectors passing through the source has the advantage to be a fixed system and can be used for one-sided massive objects. This modality leads to a RT on a family of circular arcs with a common fixed extremity (the point source) and the other extremity point is located on the detector line. An improved version of this modality with a double scanning[14] has been also proposed. For biomedical imaging and small objects scanning, a CST modality, proposed by Nguyen,[15,16] is composed of a pair source–detector diametrically opposed on a circle. The pair source–detector rotates around its fixed axis during the imaging process. Data acquisition and image reconstruction of this system is modeled by a RT on a family of circular arcs having a chord of fixed length.

1.4 *Motivation of This Work and Outline of the Paper*

The purpose of this paper is to propose and study new potentials of a CST modality named circular Compton scattering tomography (CCST) recently proposed in Refs. 17–20. Here the objective is explore the possibility for the same system to scan both small and large objects. Thus with the same system, both kinds of applications either biomedical imaging or nondestructive evaluation can be performed, enlarging in this way fields of applications for the same CST system. In this context, the modeling of these two scanning modes is studied in this paper.

This paper is organized as follows: Sec. 2 presents the new imaging system with its double scanning configuration and gives working assumptions of this study. Section 3 describes the modeling of the two possible modes of acquisition, internal scanning and external scanning, which leads to a RT on a new family of circular arcs never studied before. This new RT is named CirArcRT in the remainder of the paper. We will see that the CirArcRT can be inverted via geometrical inversion, leading to a Radon transform on half-lines (HLineRT). Inversion of the HLineRT is established in Sec. 5. The complete general algorithm for image reconstruction and simulation results for the two scanning modes are presented in Sec. 6. Perspectives of this work are proposed in Sec. 7.

2 Presentation of the System Circular Compton Scattering Tomography and Its Double Scanning Mode

CCST has been recently proposed in Refs. 17–20 with the first objective to merge both advantages of previous ones, that is a fixed system (which avoids a cumbersome mechanical rotation) while being convenient for biomedical imaging. Before introducing double scanning mode, the two next paragraphs remind us of on the geometry of CCST and provide working assumptions for the study of this modality.

2.1 *Geometry of the New System and Its Advantages*

The proposed modality is made of a fixed source and a ring of detectors passing through the source. Without any motion of the system source–detectors, this new modality can collect a complete set of projections, useful for image reconstruction. Moreover, designing a system with multiple detectors like CCST allows making the acquisition time shorter and then reducing the radiation dose.

2.2 *General Assumptions for This Study*

This study is part of a mathematical approach to validate from a theoretical point of view the feasibility of this new system. Consequently, as in other publications about CST systems,[13–20] the model is idealized in the sense as follows.

- First-order scattering is dominant in comparison to higher order scattering.
- Compton scattering is the unique physical interaction responsible for radiation attenuation.
- Both scanning modes use idealized source and detectors with a perfect collimation.

Considering these assumptions, modeling data acquisition for CCST leads to a RT on the family of circular arcs having a common fixed extremity (the point source) and the other endpoint is located on a circle (the ring of detectors). Image reconstruction requires the inversion of the CirArcRT. This RT and its inversion, proposed here, have never been studied elsewhere and are completely different from previous works[17,18,20] about CCST.

The procedure for inversion uses geometric inversion (GI) to convert the CirArcRT into a HLineRT, whose inversion is derived from the work about the half-space RT.[21]

2.3 *First Scanning Mode for Small Objects: Internal Scanning*

The first scanning mode concerns small objects that can be placed inside the ring of detectors. Figure 2 shows this internal scanning mode, with the concerned set of circular arcs for a particular scattering angle ω.

2.4 *Second Scanning Mode for Large Objects: External Scanning*

The second mode is the external scanning, with the object placed next to the ring of detectors. This mode can be used for large objects, which cannot be placed inside the ring of detectors. Figure 3 illustrates the external scanning mode and the set of circular arcs used for image acquisition is shown for a particular scattering angle ω.

3 Modeling of CCST and Its Two Acquisition Modes of Circular Compton Scattering Tomography

3.1 *Setup of the Fixed System*

Considering a source S, placed at the origin of the coordinates system, the polar equation of the detectors ring (in black in Figs. 2–5) passing through the source is

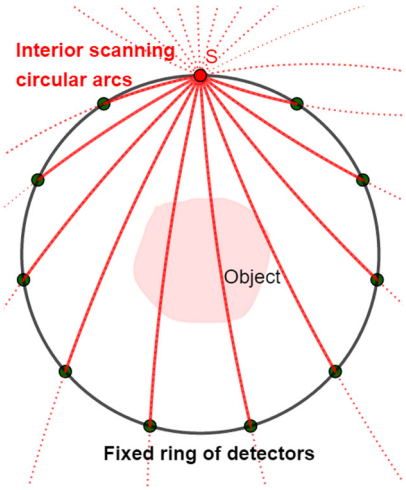

Fig. 2 Internal scanning of the CCST modality. In red: set of scanning circular arcs for an arbitrary angle ω.

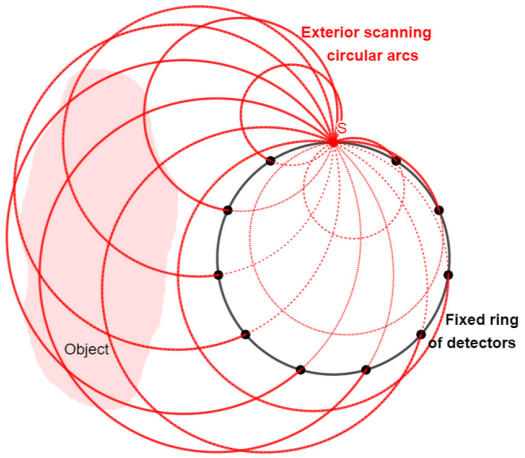

Fig. 3 External scanning of the CCST modality. Plain red curves: set of scanning circular arcs for an arbitrary angle ω. Dotted curves: rest of supported circle not used for data acquisition.

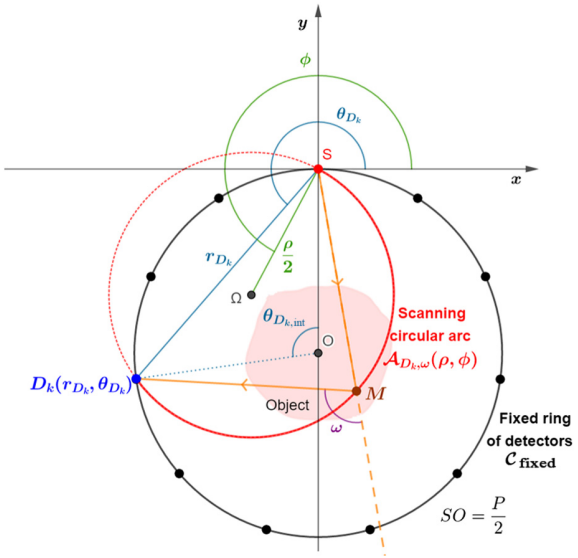

Fig. 4 Modeling of internal scanning.

$$\forall\ \theta \in [\pi, 2\pi[, \quad \mathcal{C}_{\text{fixed}}\colon\ r = P \cdot \cos\left(\theta + \frac{\pi}{2}\right), \tag{2}$$

where P is the diameter of the ring.

K detectors D_k, $k \in \{1, \ldots, K\}$ and the source S are equally spaced on the ring. This point is achieved defining first the angle subtending the y axis and OD_k, denoted $\theta_{D_{k,\text{int}}}$ for each detector D_k

$$\theta_{D_{k,\text{int}}} = 2\pi \frac{k}{K+1}, \tag{3}$$

and related with the angular polar coordinates of D_k by

$$\theta_{D_k} = \pi + \frac{\theta_{D_{k,\text{int}}}}{2}. \tag{4}$$

Hence, polar coordinates (r_{D_k}, θ_{D_k}) of detector D_k are

$$D_k(r_{D_k}, \theta_{D_k}) \text{ with } \begin{cases} r_{D_k} = P \cos\left(\theta_{D_k} + \frac{\pi}{2}\right) \\ \theta_{D_k} = \pi\left(1 + \frac{k}{K+1}\right). \end{cases} \tag{5}$$

3.2 *Characterizing the Circular Arcs for the Internal Scanning*

Given a detector $D_k(r_{D_k}, \theta_{D_k})$ and an arbitrary angle $\omega \in]0, \pi[$, the corresponding scanning circular arc $\mathcal{A}$ is characterized in polar coordinates by its diameter $\rho(D_k, \omega)$ and the angle between the x axis and its radius passing through the origin $\Phi(D_k, \omega)$. An example of these circular arcs $\mathcal{A}_{D_k,\omega}(\rho, \phi)$ is shown in plain red for internal scanning in Fig. 4.

The family of circular arcs, considered here, has the common endpoint S, the origin of the coordinate system. Consequently, this family of circular arcs is a subfamily of the family of circles passing through the origin, with the variable θ going through a limited domain $[\theta_1(D_k, \omega), \theta_2(D_k, \omega)]$ [whereas $[\pi, 2\pi[$ is the domain for the whole circle supporting the considered scanning arc]:

$$\mathcal{A}_{D_k,\omega}(\rho, \phi): \; r = \rho \cdot \cos(\theta - \phi), \quad \theta \in [\theta_1(D_k, \omega), \theta_2(D_k, \omega)], \tag{6}$$

where

$$\begin{cases} \rho(D_k, \omega) = \frac{r_{D_k}}{\sin(\omega)} \\ \phi(D_k, \omega) = \theta_{D_k} + \omega - \frac{\pi}{2}, \end{cases} \tag{7}$$

and the domain of θ is

$$\theta \in \begin{cases} [\theta_{D_k}, \theta_{D_k} + \omega] & \text{if } \phi \in [0, \frac{3\pi}{2}[\\ [\theta_{D_k} + \omega, \theta_{D_k} + \pi] & \text{if } \phi \in [\frac{3\pi}{2}, 2\pi[. \end{cases} \tag{8}$$

3.3 *Characterizing the Circular Arcs for the External Scanning*

The general parametrization of the system for external scanning is illustrated in Fig. 5.

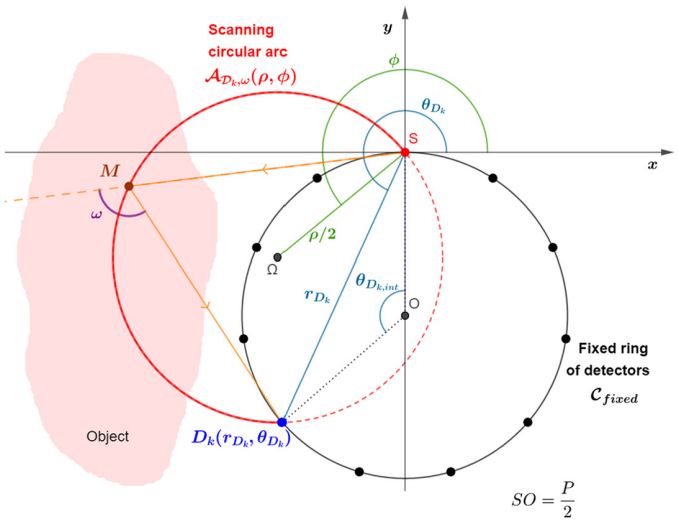

Fig. 5 Modeling of external scanning.

The scanning arcs for the external scanning mode derive from the same family of circles passing through the origin [see Eq. (6)], where $[\theta_1(D_k,\omega),\theta_2(D_k,\omega)]$ describes the complementary domain of the internal scanning one

$$\theta \in \begin{cases} [\theta_{D_k}+\omega,\theta_{D_k}+\pi] & \text{if } \phi \in [0,\frac{3\pi}{2}[\\ [\theta_{D_k},\theta_{D_k}+\omega] & \text{if } \phi \in [\frac{3\pi}{2},2\pi[. \end{cases} \tag{9}$$

4 Corresponding Radon Transform on Circular Arcs

From the previous paragraphs, one can see that modeling data acquisition for either internal or external scanning differs one to the other only from the domain of θ and consequently leads to the same RT on circular arcs named CirArcRT. This is why equations of image acquisition and reconstruction of the CirArcRT will be established once in this section. In the remainder of this paper, the family of circular arcs corresponding to internal (resp. external) scanning will be denoted interior (resp. exterior) circular arcs according to their position relative to the fixed ring of detectors.

4.1 *Image Acquisition*

In the remainder of this paper, f represents the object to scan and denotes a non-negative, continuous, and compactly supported unknown function. The CirArcRT of f is

$$\mathcal{R}_{\text{CirArc}}f(\rho,\phi)=\int_{\mathcal{A}_{D_k,\omega}(\rho,\phi)} f(r,\theta)\mathrm{d}s, \tag{10}$$

where s being a parameter associated to the circular arc $\mathcal{A}_{D_k,\omega}(\rho,\phi)$. Equation (10) is the image acquisition equation for internal and external scanning.

Another writing for the CirArcRT is

$$\mathcal{R}_{\text{CirArc}}f(\rho,\phi)=\int_{-\infty}^{\infty}\int_{\theta_1}^{\theta_2}\rho f(r,\theta)\delta[r-\rho\,\cos(\theta-\phi)]\mathrm{d}r\,\mathrm{d}\theta, \tag{11}$$

where $[\theta_1,\theta_2]$ describes the considered domain of θ either for internal or external scanning case.

Equation (11) of image formation with the use of a delta function kernel shows the difficulty to inverse stably the CirArcRT in the case of missing data and/or noise.

4.2 *Inverting the CirArcRT*

Image reconstruction requires the inversion of the CirArcRT. However, the analytic inversion of the CirArcRT has not been found at present. We will proceed via GI, a planar transformation that converts circular arcs in half lines. Consequently, this transformation allows us to convert our circular arc RT in a RT on a family of half-lines never made explicit before, and the inversion of this new RT is established in the next section.

4.3 *Geometric Inversion of the Families of Interior and Exterior Circular Arcs*

GI is characterized in polar coordinates by the change of variables:

$$r'=q^2/r, \tag{12}$$

where q is the module of inversion.

Then using Eq. (12) in Eq. (6), one can obtain

$$\rho'=r'\,\cos(\theta-\phi)\quad \text{where } \rho'=q^2/\rho\quad \text{and}\quad \theta\in[\theta_1,\theta_2]. \tag{13}$$

As our families of interior and exterior circular arcs have the origin as their common extremity point, this point will be rejected to infinity after GI. Furthermore, the other extremity points, located before GI on a circle, are now on a straight line. Considering these two points, one can see that Eq. (13) is an equation of a half line of polar parameters (ρ',ϕ).

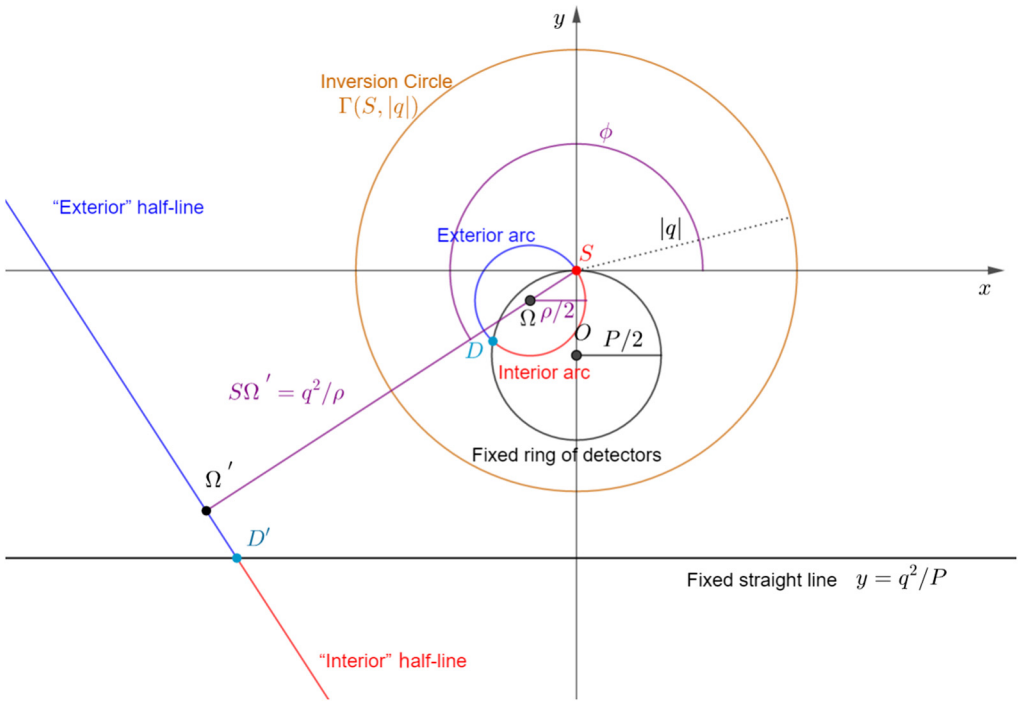

Fig. 6 GI of the interior and exterior circular arcs.

Another method to characterize the obtained family of half-lines is to proceed schematically (see Fig. 6). In fact, GI is characterized geometrically by an inversion circle [denoted $\Gamma(S, |q|)$, in brown] with its centre S at the origin of the coordinate system and radius $|q|$, with $q \in \mathbb{R}^*$.

Figure 6 illustrates the process of GI of our families of circular arcs into half-lines, with an example for each scanning case. The fixed detector ring is represented by the fixed circle in black. The next paragraphs describe GI for the two scanning cases and for the fixed setup.

4.3.1 *Geometric inversion of the fixed setup*

The fixed ring of detector is converted into a fixed horizontal line of the plane and shows the location of the apparent detectors after GI. As an example, in Fig. 6, the apparent detector D' corresponds to the GI of the detector D.

4.3.2 *Geometric inversion of the interior arcs*

For the particular detector D (in light blue), an example of interior arc is represented in red. Then by GI, the interior arc is converted into the red half-line located above the black line.

More generally, interior arcs will be converted into half-lines having their extremity on the black line and located above it. For the sake of continuity, half-lines corresponding to internal scanning will be called interior half-lines.

4.3.3 *Geometric inversion of the exterior arcs*

For the same detector D, an example of exterior arc is represented in blue. Similar to the internal case, this exterior arc is converted into an half-line, but this half-line is located below the line of detectors. By analogy, the family of exterior arcs becomes by GI the family of half-lines located below the line of apparent detectors.

4.3.4 *Toward a new family of half-lines*

Consequently, the internal scanning and the external scanning lead to an RT on a family of half-lines located below or above a horizontal line of the plane. The equation of this fixed straight line

is relative to the choice of the radius of the inversion circle $|q|$ and P the diameter of the fixed detectors ring in Cartesian coordinates: $y = q^2/P$.

A previous work of Truong and Nguyen[21] studies the inversion of the RT in half space. This corresponds to our family of half-lines with the x axis as the fixed dividing line. We will generalize this work in order to invert the RT on our family of half-lines, named HLineRT, considering any arbitrary fixed horizontal line separating the plane. This horizontal line will contain the extremities of half-lines.

4.4 *Relation Between the CirArcRT and the HLineRT*

Applying the change of variables $r' = q^2/r$ to Eq. (11), one can obtain

$$\mathcal{R}_{\text{CirArc}} f(\rho, \phi) = \int_{\mathbf{R}^+ \times (\theta_1, \theta_2)} r' \frac{q^2}{r'^2} f\left(\frac{q^2}{r'}, \theta\right) \cdot \delta[\rho' - r' \cos(\theta - \phi)] \mathrm{d}r' \, \mathrm{d}\theta. \tag{14}$$

Consequently, by GI, the CirArcRT of a function f leads to a the HLineRT of an apparent function denoted by f_{app}

$$\mathcal{R}_{\text{CirArc}} f(\rho, \phi) = \mathcal{R}_{\text{HLine}} f_{\text{app}}\left(\frac{q^2}{\rho}, \phi\right), \tag{15}$$

where f_{app} is the GI of f, weighted by q^2/r^2:

$$f_{\text{app}}(r, \theta) = \frac{q^2}{r^2} f\left(\frac{q^2}{r}, \theta\right). \tag{16}$$

5 Inverting the Radon Transform on Half-Lines

As the RT in our modality is the HLineRT of a part of the space 2-D delimited by the lowest or the highest values by a horizontal straight line, it is more convenient to consider the situation in Cartesian coordinates with the parametrization proposed in Fig. 7.

Moreover, for $a \in \mathbf{R}$, $y = a$ represents the equation of the horizontal fixed straight line of detectors. Consequently, $\mathcal{R}_{\text{Hline}}$ is renamed $\mathcal{R}_a^+$ and $\mathcal{R}_a^-$ according to their reference for half-lines located, respectively, below and under the considered horizontal line.

Thus using the change of variables associated to Fig. 7:

$$\tau = \tan \phi, \quad \xi = \frac{\rho}{\cos \phi}, \quad \mathrm{d}\xi \, \mathrm{d}\tau = \frac{1}{\cos \phi} \mathrm{d}\rho \, \mathrm{d}\phi, \tag{17}$$

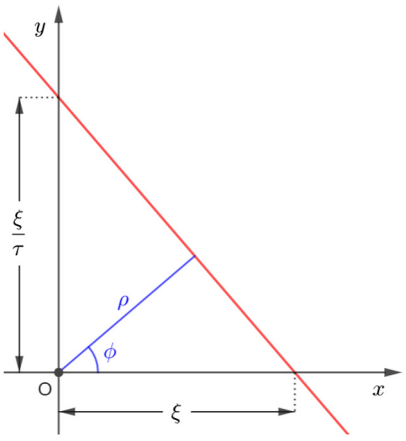

Fig. 7 Chosen parameters for a straight line in Cartesian coordinates.

$\mathcal{R}_a^- f_{\text{app}}$ and $\mathcal{R}_a^+ f_{\text{app}}$ are, respectively, written in Cartesian coordinates:

$$\mathcal{R}_a^- f_{\text{app}}(\xi,\tau) = \int_{-\infty}^{a} \mathrm{d}y \sqrt{1+\tau^2} f_{\text{app}}(\xi - y\tau, y) \tag{18}$$

and

$$\mathcal{R}_a^+ f_{\text{app}}(\xi,\tau) = \int_{a}^{\infty} \mathrm{d}y \sqrt{1+\tau^2} f_{\text{app}}(\xi - y\tau, y). \tag{19}$$

After calculations (summed up in Sec. 9), apparent function f_{app} can be entirely recovered from projections of, respectively, $\mathcal{R}_a^- f_{\text{app}}$ and $\mathcal{R}_a^+ f_{\text{app}}$ using, the equations:

$$f_{\text{app}}(x,y) = \frac{1}{2\pi^2} H_a^-(y) \quad \text{p.v.} \int_{\mathbf{R}^2} \frac{\mathrm{d}\tau \mathrm{d}\xi}{\sqrt{1+\tau^2}} \frac{1}{(\xi - \tau y - x)} \frac{\partial}{\partial \xi} \mathcal{R}_a^- f_{\text{app}}(\xi,\tau) \tag{20}$$

and

$$f_{\text{app}}(x,y) = \frac{1}{2\pi^2} H_a^+(y) \quad \text{p.v.} \int_{\mathbf{R}^2} \frac{\mathrm{d}\tau\, \mathrm{d}\xi}{\sqrt{1+\tau^2}} \frac{1}{(\xi - \tau y - x)} \frac{\partial}{\partial \xi} \mathcal{R}_a^+ f_{\text{app}}(\xi,\tau), \tag{21}$$

where p.v. denotes the Cauchy principal value.

Then considering the change of variables

$$\phi = \tan^{-1}\tau, \quad s = \frac{\xi}{\sqrt{1+\tau^2}} \quad \text{and} \quad \mathrm{d}s\, \mathrm{d}\phi = \frac{1}{(1+\tau^2)^{\frac{3}{2}}} \mathrm{d}\xi\, \mathrm{d}\tau, \tag{22}$$

inverse equations of $\mathcal{R}_a^- f_{\text{app}}$ [Eq. (21)] and $\mathcal{R}_a^+ f_{\text{app}}$ [Eq. (20)] are, respectively, expressed with acquired data in polar coordinates

$$f_{\text{app}}(x,y) = \frac{1}{2\pi^2} H_a^-(y) \int_0^{2\pi} \mathrm{d}\phi \quad \text{p.v.} \left[\int_0^{\infty} \frac{\mathrm{d}\rho}{\rho - x\cos\phi - y\sin\phi} \frac{\partial}{\partial \rho} \mathcal{R}_a^- f_{\text{app}}(\rho,\phi) \right] \tag{23}$$

and

$$f_{\text{app}}(x,y) = \frac{1}{2\pi^2} H_a^+(y) \int_0^{2\pi} \mathrm{d}\phi \quad \text{p.v.} \left[\int_0^{\infty} \frac{\mathrm{d}\rho}{\rho - x\cos\phi - y\sin\phi} \frac{\partial}{\partial \rho} \mathcal{R}_a^+ f_{\text{app}}(\rho,\phi) \right]. \tag{24}$$

Finally, the function f is recovered from f_{app} with the equation

$$f(r,\theta) = \frac{q^2}{r^2} f_{\text{app}}\left(\frac{q^2}{r}, \theta\right), \tag{25}$$

in polar coordinates and the equation

$$f(x,y) = \frac{q^2}{x^2+y^2} f_{\text{app}}\left(\frac{q^2 x}{x^2+y^2}, \frac{q^2 y}{x^2+y^2}\right) \tag{26}$$

in Cartesian coordinates.

6 General Reconstruction Algorithm and Numerical Simulation Results

This section gives details about practical simulations of internal and external scanning modes for CCST. These simulations are performed under the conditions stated in Sec. 2.2 in order to validate the analytic inversion procedure for the CirArcRT for this first study and the theoretical feasibility of CCST, in the sense that this system is able to recover sufficient data for reconstruction. Some works are on the way in order to approach realistic measurements. This point is discussed in Sec. 7.

Simulations have been performed with MATLAB R2018b.

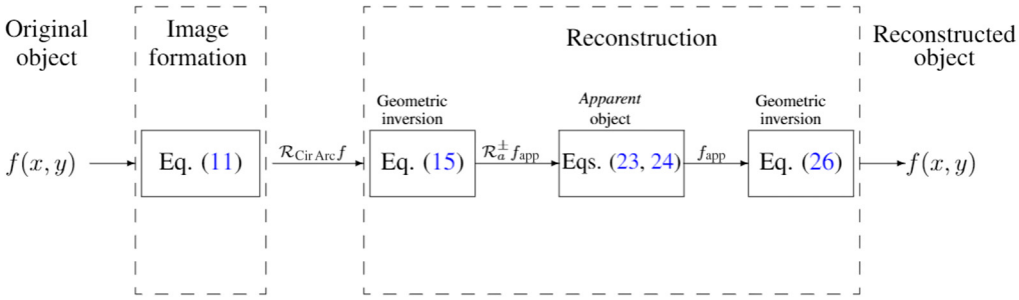

Fig. 8 General algorithm for image reconstruction.

6.1 *General Reconstruction Algorithm*

First, the general algorithm is summed up in Fig. 8.

6.2 *Step 1: Parameter Choices*

For simulations, the parameters that have to be chosen are: P the diameter of the fixed ring of detectors, N_D the number of detectors placed on the ring, $N_\omega = N_\phi$ the number of scanning arcs per detector, and $|q|$ the radius of the inversion circle.

Broadly speaking, N_D and N_ϕ have to satisfy the well-known condition given in Ref. 22 and reformulated in our case as

$$N_D \times N_\phi > N_1 \times N_2, \tag{27}$$

where (N_1, N_2) represents the size of the scanned object.

This condition allows having the lower limitation of required parameter numbers for data acquisition, in an idealized case of uniform sampling, without perturbations like missing data or noise. However, the condition of data sampling is not respected because data are acquired on circular arcs. This is why parameters N_ϕ and N_D have to be overestimated.

The choice of the parameter $|q|$ of GI does not influence the quality of reconstruction. It has just to be chosen to encompass the whole system and the object inside the inversion circle.

6.2.1 *Parameter choices for the fixed setup: choice of N_ϕ, N_D, and P*

The main objective of these simulations is to show the ability for the same system (same size of ring and same number of detectors) to reconstruct both small and large objects. Consequently, P, N_D, and N_ϕ are chosen once for all presented simulations. $N_D = 3217$ detectors are equally placed on a ring of diameter $P = 1024$. This represents one detector per unit length. For the projections, we take $N_\phi = 3000$ in order to satisfy Eq. (27).

6.2.2 *Parameter choices and chosen objects for internal scanning*

Internal scanning is performed for two objects, the medical Shepp–Logan phantom and a defected connector. The objective is to verify the ability for CCST to reconstruct small details as the welding defect [framed in red in Fig. 9(a)] of the connector and small nodules of Shepp–Logan [Fig. 10(a)]. The size of these objects is $N \times N = 512 \times 512$ that is smaller than the ring of detectors. The radius of the inversion circle is $|q| = 1100$. Simulation results are presented for the connector and for Shepp–Logan phantom, respectively, in Figs. 9 and 10.

6.2.3 *Parameter choices and chosen objects for external scanning*

External scanning is also performed for two objects, a test object with multiple layers [Fig. 11(a)], previously used in Ref. 10) and a cracked bar [Fig. 12(a)]. Here the objective

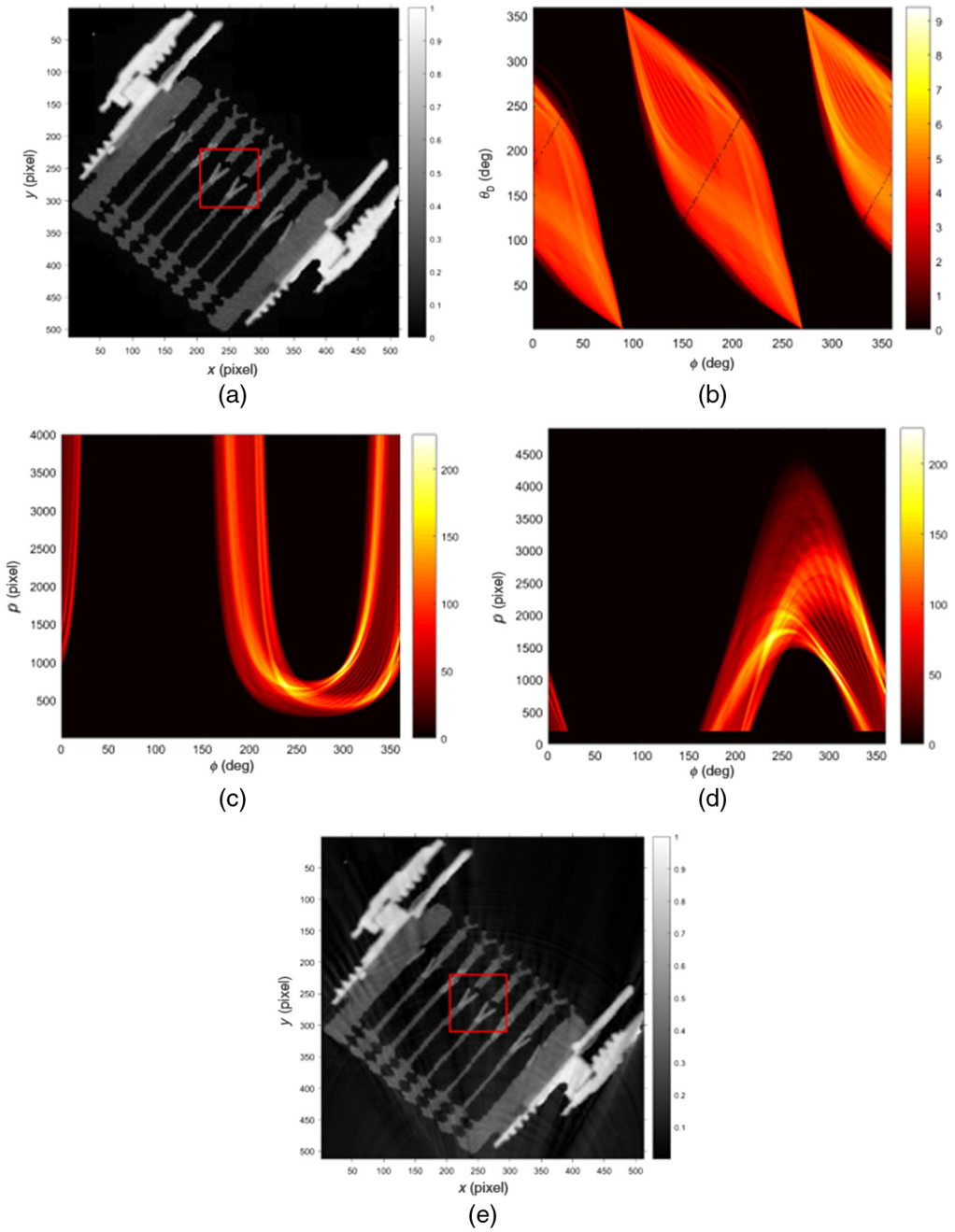

Fig. 9 Interior scanning: (b) data acquisition, (c) rearranged data, (d) GI, and (e) image reconstruction of a connected defector (a) (NMSE = 0.0039).

is to verify the ability for CCST to be able to reconstruct larger objects than the ring, in this case, object of size $N_1 \times N_2 = 1200 \times 360$. The radius of the inversion circle is $|q| = 1500$. Simulation results are presented for the phantom with multiple layers and for the cracked bar, respectively, in Figs. 11 and 12.

6.3 *Step 2: Image Formation*

Data of the original object are acquired first according to the parameters of the scanning circular arcs $\theta_{D_{k,\text{int}}}$ and ϕ. The parameter $\theta_{D_{k,\text{int}}}$ allows choosing the considered detector and ϕ, which is related to ω, allows specifying the scanning circular arc.

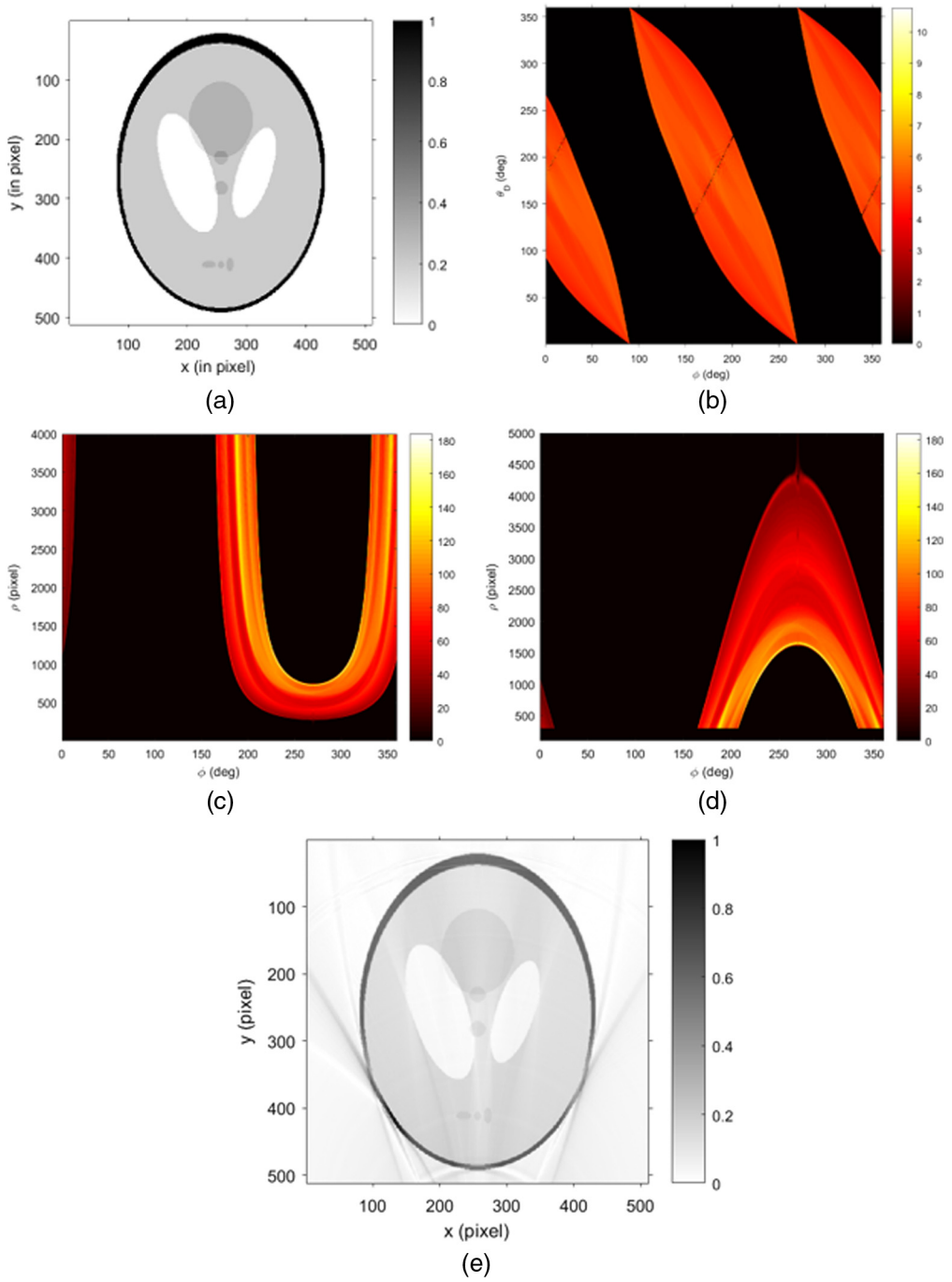

Fig. 10 Interior scanning: (b) data acquisition, (c) rearranged data, (d) GI, and (e) image reconstruction of Shepp–Logan phantom (a) (NMSE = 0.014).

Then, denoting ϕ_l the discretized version of ϕ, scanning arcs are parametrized in Cartesian coordinates as follows for simulations:

$$\mathcal{A}(\theta_{D_k}, \phi_l): \begin{cases} x(\gamma) = \frac{\rho(\theta_{D_k}, \phi_l)}{2} [\cos(\gamma) + \cos(\phi_l)] \\ y(\gamma) = \frac{\rho(\theta_{D_k}, \phi_l)}{2} [\sin(\gamma) + \sin(\phi_l)] \end{cases}, \tag{28}$$

where the respective domain of $\gamma \in [\gamma_1, \gamma_2]$ is as follows.

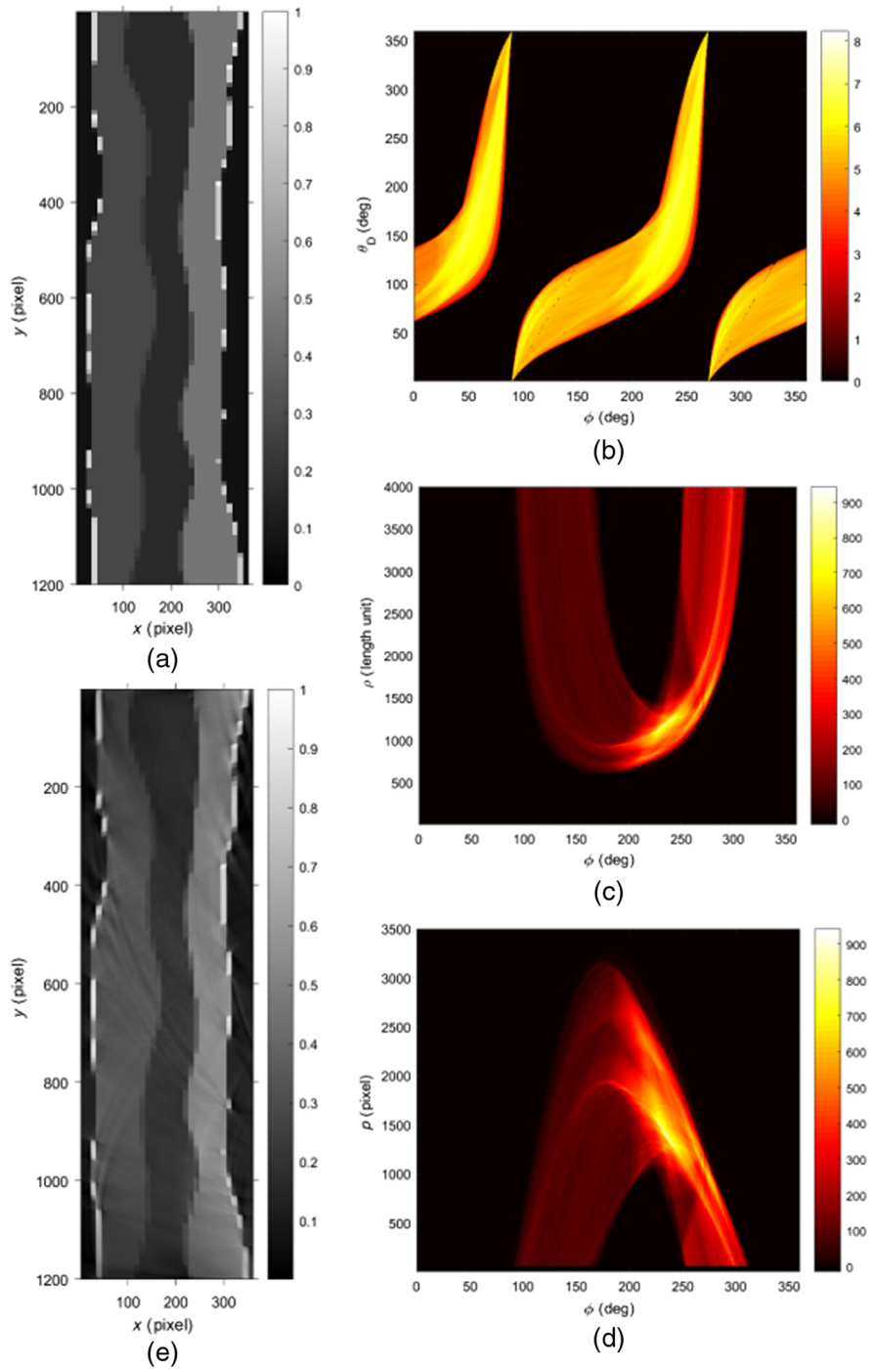

Fig. 11 Exterior scanning: (b) data acquisition, (c) rearranged data, (d) GI, and (e) image reconstruction of a multilayer phantom (a) (NMSE = 0.044).

- For the internal scanning case:

$$\gamma \in \begin{cases} [\phi_l - 2\omega - \pi, \phi_l - \pi] & \text{if } \phi \in [0, \frac{3\pi}{2}[\\ [\phi_l - \pi, \phi_l - 2\omega + \pi)] & \text{if } \phi \in [\frac{3\pi}{2}, 2\pi[\end{cases}, \tag{29}$$

- For the external scanning case:

$$\gamma \in \begin{cases} [\phi_l + \pi, \phi_l - 2\omega + \pi] & \text{if } \phi \in [0, \frac{3\pi}{2}[\\ ([\phi_l - 2\omega - \pi, \phi_l - \pi] & \text{if } \phi \in [\frac{3\pi}{2}, 2\pi[. \end{cases} \tag{30}$$

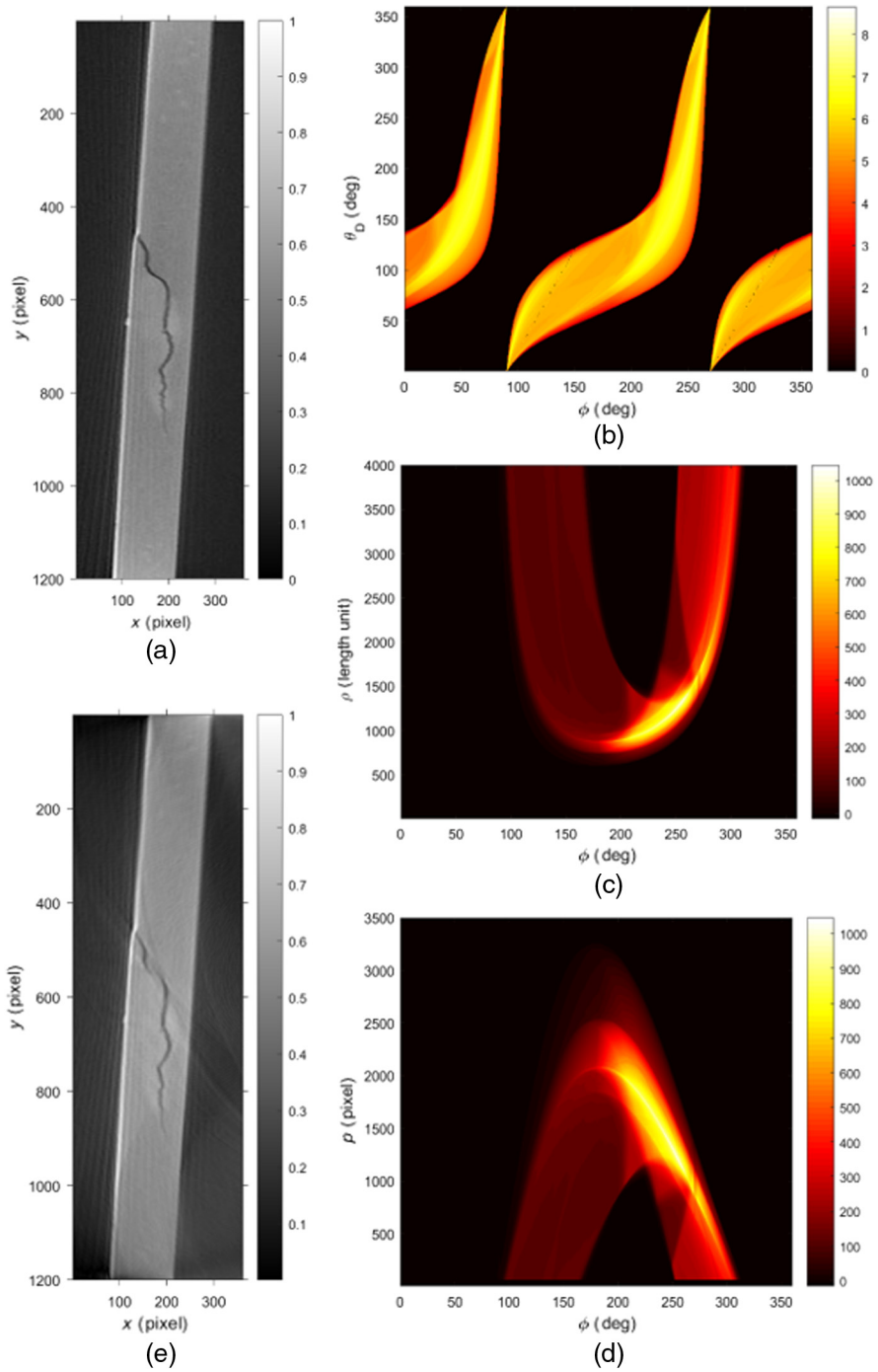

Fig. 12 Exterior scanning: (b) data acquisition, (c) rearranged data, GI (d) and image reconstruction (e) of a cracked bar (a) (NMSE = 0.055).

Consequently, the integral for image acquisition is also reformulated in Cartesian coordinates. One gets

$$\mathcal{R}_{\mathrm{CirArc}} f(\theta_{D_k}, \phi_l) = \frac{\rho(D_k, \phi_l)}{2} \int_{\gamma_1}^{\gamma_2} f[x(\gamma), y(\gamma)] \mathrm{d}\gamma. \tag{31}$$

For each scanning arc $\mathcal{A}(D_k, \phi)$, we obtain by interpolation the pairs (x, y) belonging to both the object and $\mathcal{A}(D_k, \phi)$. These pairs are integrated via a discrete trapezoidal integration and the result, weighted by $\rho(D_k, \phi_l)/2$, forms the projection $\mathcal{R}_{\mathrm{CirArc}}(\theta_D, \phi)$.

Algorithm 1 Image formation on circular arcs.

Data: Original object $f(x,y)$

Result: Data acquisition $\mathcal{R}_{\text{CirArc}} f(\theta_{D_{k,\text{int}}}, \phi)$

1 Choice of N_D the number of detectors and N_ϕ the number of scanning arcs per detector;

2 Computation of discrete variables θ_{D_k} and ϕ_l as follows:

$$\theta_{D_k} = \pi\left(1 + \frac{k}{N_D + 1}\right) \quad \text{and} \quad \phi_l = \frac{2\pi l}{N_\phi} \tag{32}$$

for ***each*** $pair(\theta_{D_k}, \phi_l)$ **do**

3 Computation of the pairs (x,y) of the Cartesian parametrization of $\mathcal{A}(\theta_{D_k}, \phi_l)$ [Eq. (28)];

4 Interpolation with the position of object f;

5 Trapezoidal integration and weight the result by $\rho(D_k, \phi_l)/2$ to obtain $\mathcal{R}_{\text{CirArc}}(\theta_{D_k}, \phi_l)$;

6 **end**

Algorithm 1 summarizes the computation steps to obtain data acquisition of an object f.

Then obtained data $\mathcal{R}_{\text{CirArc}}(\theta_{D_{k,\text{int}}}, \phi)$ need to be interpolated to have data acquisition relative to (ρ, ϕ). This process allows having after GI data projection on half-lines according to (ρ, ϕ).

6.4 *Step 3: Geometric Inversion of Acquired Data*

Acquired data are transposed to a projection on half-lines via GI with Eq. (15).

6.5 *Step 4: Reconstruction of the Apparent Object*

The apparent object is recovered with the inverse HLineRT expressed by Eqs. (23) and (24).

For simulations, these equations are reformulated with the Hilbert transform, defined as follows:

$$\mathcal{H}\{u\}(t) = \frac{1}{\pi} \quad \text{p.v.} \left[\int_{-\infty}^{\infty} \frac{u(\tau)}{t-\tau} \mathrm{d}\tau\right]. \tag{33}$$

Then the Hilbert transform is computed in the Fourier domain via the following equation:

$$\mathcal{H}\left\{\frac{\partial u}{\partial t}\right\}(t) = \mathcal{F}^{-1}[|\nu| \cdot \mathcal{F}(u)(\nu)](t), \tag{34}$$

where $\mathcal{F}$ denotes the one-dimensional Fourier transform.

Final reconstruction equations for the apparent object are respectively, for the external scanning

$$f_{\text{app}}(x,y) = \frac{1}{2\pi}\int_0^{2\pi} \mathrm{d}\phi \mathcal{F}^{-1}\{|\nu|\mathcal{F}[\mathcal{R}_a^+ f_{\text{app}}(\rho,\phi)](\nu)\}(x\cos\phi + y\sin\phi) \tag{35}$$

and for the internal scanning

$$f_{\text{app}}(x,y) = \frac{1}{2\pi}\int_0^{2\pi} \mathrm{d}\phi \mathcal{F}^{-1}\{|\nu|\mathcal{F}[\mathcal{R}_a^- f_{\text{app}}(\rho,\phi)](\nu)\}(x\cos\phi + y\sin\phi). \tag{36}$$

Similar to the classical RT, Eqs. (35) and (36) need to be regularized, due to the divergence of the ramp filter for high frequencies. We use the Hamming apodization window in the Fourier

Algorithm 2 Reconstruction of apparent object.

Data: $\mathcal{R}_{\vec{a}}^{\pm} f_{\text{app}}(\rho, \phi)$, projections on half-lines of *apparent* function f_{app}

Result: $f_{\text{app}}(x, y)$

1 Filter $\mathcal{R}_{\vec{a}}^{\pm} f_{\text{app}}(\rho, \phi)$ in the Fourier domain with filter Ψ [Eq. (38)];

2 **for** ***each*** ϕ_l **do**

3 Interpolate filtered data on the considered circle of coordinates $X \cos \phi_l + Y \sin \phi_l$, where $[X, Y]$ are the matrices of Cartesian coordinates of f_{app};

4 **end**

5 Sum the interpolations;

6 Weight the result by $1/2\pi$;

domain to reduce the amplification that may be caused by the outline of the object:

$$w(\nu) = 0.54 - 0.46 \cos(2\pi\nu), \tag{37}$$

where ν is the normalized frequency. Then the new filter is

$$\Psi(\nu) = |\nu| \cdot w(\nu) = |\nu|[0.54 - 0.46 \cos(2\pi\nu)]. \tag{38}$$

This new filter Ψ replaces the ramp filter $|\nu|$ in Eqs. (35) and (36).

Algorithm 2 summarizes the different steps for reconstructing the apparent object.

6.6 *Step 6: Reconstruction of the Original Object*

The physical object $f(x, y)$ is recovered via GI of $f_{\text{app}}(x, y)$ with Eq. (26).

6.7 *Step 7: Evaluation of the Quality of Reconstruction*

We use the normalized mean square error (NMSE) defined by

$$\text{NMSE} = \frac{\sum_{(i,j)\in(|1,N_1|)\times(|1,N_2|)}[I_o(i,j) - I_r(i,j)]^2}{\max\limits_{(i,j)\in(|1,N_1|)\times(|1,N_2|)} I_o(i,j)^2} \cdot \frac{1}{N_1 N_2}, \tag{39}$$

where I_o and I_r are, respectively, the original and the reconstructed images and (N_1, N_2) is the size of the considered image.

6.8 *Discussion on Simulation Results*

Reconstruction is globally acceptable in the sense that small details are visible by internal scanning and objects larger than the system can also be reconstructed by external scanning. Furthermore, both simulations for internal and external scanning cases lead to a similar quality of reconstruction and this point ensures the independence of the chosen object to the reconstruction algorithm.

However, reconstructions have some artifacts. For example, in the case of Shepp–Logan phantom, artifacts are visible in the lower left and right edges of the object. These artifacts are due to missing data because projection on circular arcs has to be limited to a finite diameter (whereas circular arcs having an infinite diameter gives also information). The mathematical theory explaining these artefacts due to missing data is microlocal analysis. The case of the classical RT on straight lines has been studied particularly by Nosmas,[23] Krishnan, and

Quinto,[24] Frikel and Quinto,[25] and Quinto.[26] Some extra works to extend microlocal analysis theory for generalized RTs such as CirArcRT are needed.

7 Perspectives

This first work about the double scanning configuration opens new perspectives that will be part of our future works.

7.1 *Introduce Attenuation of Scattered Radiation in the Model*

In addition to scattering events, radiation is attenuated inside matter. Consequently, a more complete model for data acquisition and image reconstruction should consider also attenuation. For a CST system, this leads to an attenuated RT on the corresponding family of circular arcs, according to the geometry of the system. However, no exact inversion for this kind of RT has been found for any CST system. An alternative is to propose an algorithm that corrects iteratively reconstruction, from a error computation. Such algorithm has been proposed for the previous Nguyen and Truong modality.[27] A first work[28] on this subject has been proposed for the internal scanning of CCST in the special case of the *a priori* knowledge of the attenuation map.

7.2 *Take into Account a Practical System for Simulations to Approach Real Measurements*

A perspective of this work concerns simulations of the CCST system in more realistic conditions (particularly the properties of source and detectors such as energy range and resolution, introduce Klein–Nishina probability, and collimation at detectors). In this context, Monte Carlo simulations will be considered.

7.3 *An Extension of CCST in Three Dimensions*

An extension of CCST in three dimensions is also under study in order to take into account the Compton effect in the whole space (and not restricted in the plane). This 3-D modality will be made of a fixed source and a fixed sphere of detectors. The advantages of CCST will be preserved with this extension. Modeling image formation of this extension leads to a new RT on a family of torus having a fixed end-point (the point source) and the other is located on the sphere of detectors.

In a previous work, Webber and Lionheart,[29] Webber and Holman[30] proposed an extension of the previous Nguyen and Truong's modality, proved injectivity and stability of the associated torus transform. This work is one of the leading routes for this perspective.

8 Concluding Remarks and Perspectives

This paper introduces the two possible modes of acquisition for the CCST.

For small objects that can be placed inside the detector ring, the CCST works in interior mode. Otherwise, the CCST offers the possibility to scan large objects, in exterior mode, by placing them outside the detectors ring.

Moreover, the circular geometry of this new system offers the advantage to be fixed while collecting a complete data set necessary for image reconstruction and reducing the data acquisition time.

The CCST enlarges the application fields for the same system from biomedical imaging to nondestructive evaluation (detection of welding defects in a printed circuit board and detection of defaults on metallic pieces, for instance) and historical exploration (cultural heritage objects research).

The modeling of the proposed CCST leads to a new generalized CirArcRT whose inversion is possible via GI. In fact, after GI the considered CirArcRT is reduced to the HLineRT whose inversion formula has been established and inverted for the first time in this paper. This mathematical result allows solving the theoretical challenge raised by CCST.

The simulation results for internal and external scanning are promising and supporting the theoretical feasibility of the proposed CCST with a double scanning configuration.

9 Appendix A: Inversion of the Radon Transform of Half-Lines

We will only inverse $\mathcal{R}^{a^+}f$, the proof for $\mathcal{R}^{a^-}f$ is completely similar.

First, we reformulate Eq. (19) as follows:

$$\frac{\mathcal{R}^{a^+}f(\xi,\tau)}{\sqrt{1+\tau^2}} = \int_a^\infty \mathrm{d}y f(\xi - y\tau, y). \tag{40}$$

Replacing $f(x,y)$ by its representation in the Fourier domain $\tilde{f}(x,y)$ as

$$f(x,y) = \int_{\mathbf{R}^2} \mathrm{d}p\,\mathrm{d}q e^{2i\pi(px+qy)}\tilde{f}(p,q), \tag{41}$$

one gets

$$\frac{\mathcal{R}^{a^+}f(\xi,\tau)}{\sqrt{1+\tau^2}} = \int_{\mathbf{R}^2} \mathrm{d}p\,\mathrm{d}q\tilde{f}(p,q)e^{2i\pi p\xi}\int_a^\infty \mathrm{d}y e^{-2i\pi y(p\tau-q)}. \tag{42}$$

Moreover,

$$\int_a^\infty \mathrm{d}y e^{-2i\pi y(p\tau-q)} = \int_{-\infty}^\infty \mathrm{d}y H_a^+(y)e^{-2i\pi y(p\tau-q)},$$

where $H_a^+(y) = H(y-a)$ and H is the Heaviside step function: $H_a^+(y) = 0{,}5 + 0{,}5\cdot\mathrm{sign}(y-a)$.

Then

$$\begin{aligned}\int_a^\infty \mathrm{d}y e^{-2i\pi y(p\tau-q)} &= \frac{1}{2}\int_{-\infty}^\infty e^{-2i\pi y(p\tau-q)}\mathrm{d}y + \frac{1}{2}\int_{-\infty}^\infty \mathrm{sgn}(y-a)e^{-2i\pi y(p\tau-q)}\mathrm{d}y \\ &= \frac{1}{2}\left[\delta(p\tau-q) + \frac{e^{-2i\pi a(\tau p-q)}}{i\pi(p\tau-q)}\right].\end{aligned} \tag{43}$$

Equation (42) becomes

$$\begin{aligned}\frac{\mathcal{R}^{a^+}f(\xi,\tau)}{\sqrt{1+\tau^2}} &= \int_{\mathbf{R}^2} \mathrm{d}p\,\mathrm{d}q\tilde{f}(p,q)e^{2i\pi p\xi}\cdot\frac{1}{2}\left[\delta(p\tau-q) + \frac{e^{-2i\pi a(\tau p-q)}}{i\pi(p\tau-q)}\right] \\ &= \frac{1}{2}\left[\int_{\mathbf{R}}\mathrm{d}p\tilde{f}(p,\tau p)e^{2i\pi p\xi} + \int_{\mathbf{R}}\mathrm{d}p\,\mathrm{d}q\frac{1}{i\pi}\frac{\tilde{f}(p,q)}{p\tau-q}e^{2i\pi p\xi}\cdot e^{-2i\pi a(p\tau-q)}\right].\end{aligned}$$

Applying the Fourier transform on ξ on both sides of the equation, one gets

$$\int_{\mathbf{R}}\mathrm{d}\xi e^{-2i\pi\xi p}\frac{\mathcal{R}^{a^+}f(\xi,\tau)}{\sqrt{1+\tau^2}} = \frac{1}{2}\left[\tilde{f}(p,\tau p) + \frac{1}{i\pi}\int_{\mathbf{R}}\mathrm{d}q\frac{1}{i\pi}\frac{\tilde{f}(p,q)}{p\tau-q}\cdot e^{-2i\pi a(p\tau-q)}\right]. \tag{44}$$

Denoting

$$\tilde{f}(p,q) = \int_{\mathbf{R}}\mathrm{d}\xi e^{-2i\pi\xi q}g(p,\xi), \tag{45}$$

and considering the change of variables $u = p\tau - q$, the second part of Eq. (44) can be rewritten as

$$\int_{\mathbf{R}} \mathrm{d}q \frac{\tilde{f}(p,q)}{p\tau - q} e^{-2i\pi a(p\tau - q)} = \int_{\mathbf{R}} \mathrm{d}\xi e^{2i\pi\xi p\tau} g(p,\tau) \int_{\mathbf{R}} \mathrm{d}u \frac{e^{2i\pi(\xi - a)u}}{u}$$
$$= \int_{\mathbf{R}} \mathrm{d}\xi e^{2i\pi\xi p\tau} g(p,\tau) \cdot i\pi \mathrm{sgn}(\xi - a).$$

Thereby,

$$\int_{\mathbf{R}} \mathrm{d}\xi e^{-2i\pi\xi p} \frac{\mathcal{R}^{a^+} f(\xi,\tau)}{\sqrt{1+\tau^2}} = \frac{1}{2} \int_{\mathbf{R}} \mathrm{d}\xi e^{-2i\pi\xi p\tau} g(p,\xi)[1 + \mathrm{sgn}(\xi - a)],$$
$$= \int_{\mathbf{R}} \mathrm{d}\xi e^{-2i\pi\xi p\tau} H_a^+(\xi) g(p,\xi). \tag{46}$$

For $p \in \mathbf{R}$, multiplying Eq. (46), by $\int_{\mathbf{R}} \mathrm{d}(\tau p) e^{2i\pi\tau pz}$, one gets

$$\int_{\mathbf{R}} \mathrm{d}(\tau p) e^{2i\pi\tau pz} \int_{\mathbf{R}} \mathrm{d}\xi e^{-2i\pi\xi p} \frac{\mathcal{R}^{a^+} f(\xi,\tau)}{\sqrt{1+\tau^2}} = \int_{\mathbf{R}} \mathrm{d}(\tau p) e^{2i\pi\tau pz} \int_{\mathbf{R}} \mathrm{d}\xi e^{-2i\pi\xi p\tau} H_a^+(\xi) g(p,\xi)$$
$$= \int_{\mathbf{R}} \mathrm{d}\xi H_a^+(\xi) g(p,\xi) \int_{\mathbf{R}} \mathrm{d}(\tau p) e^{2i\pi\tau p(z-\xi)},$$
$$= \int_{\mathbf{R}} \mathrm{d}\xi H_a^+(\xi) g(p,\xi) \delta(z - \xi),$$
$$= H_a^+(z) g(p,z). \tag{47}$$

Then $\forall\ z > a$

$$g(p,z) = |p| \int_{\mathbf{R}^2} \frac{\mathrm{d}\tau\, \mathrm{d}\xi}{\sqrt{1+\tau^2}} e^{-2i\pi(\xi - \tau z)p} \mathcal{R}^{a^+} f(\xi,\tau), \tag{48}$$

and

$$\tilde{f}(p,q) = \int_{\mathbf{R}} \mathrm{d}z e^{-2i\pi zq} |p| \int_{\mathbf{R}^2} \frac{\mathrm{d}\tau \mathrm{d}\xi}{\sqrt{1+\tau^2}} e^{-2i\pi(\xi - \tau z)p} \mathcal{R}^{a^+} f(\xi,\tau). \tag{49}$$

From Eq. (41), we can reconstruct $f(x,y)$

$$f(x,y) = \int_{\mathbf{R}^2} \mathrm{d}p\, \mathrm{d}q e^{2i\pi(px+qy)} \int_{\mathbf{R}} \mathrm{d}z e^{-2i\pi zq} |p| \int_{\mathbf{R}^2} \frac{\mathrm{d}\tau\, \mathrm{d}\xi}{\sqrt{1+\tau^2}} e^{-2i\pi(\xi - \tau z)p} \mathcal{R}^{a^+} f(\xi,\tau). \tag{50}$$

Integrating first on $\mathrm{d}q$ and then on $\mathrm{d}z$ with $z > a$, one can find that the result is nonzero if and only if $y > a$. Then one can obtain

$$f(x,y) = H_a^+(y) \int_{\mathbf{R}^2} \frac{\mathrm{d}\tau\, \mathrm{d}\xi}{\sqrt{1+\tau^2}} \mathcal{R}^{a^+} f(\xi,\tau) \int_{\mathbf{R}} |p| \mathrm{d}p e^{-2i\pi(\xi - \tau y - x)p}. \tag{51}$$

With the Fourier table, we have

$$\int_{\mathbf{R}} |p| \mathrm{d}p e^{-2i\pi(\xi - \tau y - x)p} = \frac{-1}{2\pi^2} \frac{1}{(\xi - \tau y - x)^2}. \tag{52}$$

Hence,

$$f(x,y) = \frac{-1}{2\pi^2} H_a^+(y) \quad \text{p.v.} \left[\int_{\mathbf{R}^2} \frac{\mathrm{d}\tau\, \mathrm{d}\xi}{\sqrt{1+\tau^2}} \frac{1}{(\xi - \tau y - x)^2} \mathcal{R}^{a^+} f(\xi,\tau) \right]. \tag{53}$$

Finally, using partial integration on ξ, the reconstruction equation for an function f with the HLineRT $\mathcal{R}^{a^+} f$ is

$$f(x,y) = \frac{1}{2\pi^2} H_a^+(y) \quad \text{p.v.} \left[\int_{\mathbf{R}^2} \frac{\mathrm{d}\tau\, \mathrm{d}\xi}{\sqrt{1+\tau^2}} \frac{1}{(\xi - \tau y - x)} \frac{\partial}{\partial \xi} \mathcal{R}^{a^+} f(\xi, \tau) \right]. \tag{54}$$

Acknowledgments

This work was supported by grants from Région Ile-de-France (in Mathematics and Innovation) 2018 to 2021 and LabEx Modèles Mathématiques et Economiques de la Dynamique, de l'Incertitude et des Interactions (MME-DII) (No. ANR-11-LBX-0023-01).

References

1. J. Radon, "On the determination of functions from their integral values along certain manifolds," *IEEE Trans. Med. Imaging* **5**(4), 170–176 (1986).
2. A. M. Cormack, "Representation of a function by its line integrals, with some radiological applications," *J. Appl. Phys.* **34**(9), 2722–2727 (1963).
3. T. Truong and M. K. Nguyen, "Recent developments on Compton scatter tomography: theory and numerical simulations," in *Numerical Simulation-From Theory to Industry*, M. Andriychuk, Ed., IntechOpen, Rijeka, Croatia (2012).
4. D. L. Bailey et al., *Positron Emission Tomography*, Springer, London (2005).
5. G. Redler et al., "Compton scatter imaging: a promising modality for image guidance in lung stereotactic body radiation therapy," *Med. Phys.* **45**(3), 1233–1240 (2018).
6. K. C. Jones et al., "Characterization of Compton-scatter imaging with an analytical simulation method," *Phys. Med. Biol.* **63**(2), 025016 (2018).
7. R. H. Bossi et al., "One sided radiographic inspection using backscatter imaging," in *Review of Progress in Quantitative Nondestructive Evaluation*, D. O. Thompson and D. E. Chimenti, Eds., pp. 465–471, Springer, Boston, Massachusetts (1989).
8. S. Gautam et al., "Compton interaction tomography I. Feasibility studies for applications in earthquake engineering," *IEEE Trans. Nucl. Sci.* **30**(2), 1680–1684 (1983).
9. G. Harding and E. Harding, "Compton scatter imaging: a tool for historical exploration," *Appl. Radiat. Isot.* **68**(6), 993–1005 (2010).
10. P. G. Prado et al., "Three-dimensional imaging of flat natural and cultural heritage objects by a Compton scattering modality," *J. Electron Imaging* **26**(1), 011026 (2017).
11. E. M. Hussein, M. Desrosiers, and E. J. Waller, "On the use of radiation scattering for the detection of landmines," *Radiat. Phys. Chem.* **73**(1), 7–19 (2005).
12. P. E. Cruvinel and F. A. Balogun, "Compton scattering tomography for agricultural measurements," *Eng. Agric.* **26**(1), 151–160 (2006).
13. S. J. Norton, "Compton scattering tomography," *J. Appl. Phys.* **76**(4), 2007–2015 (1994).
14. J. Cebeiro et al., "New 'improved' Compton scatter tomography modality for investigative imaging of one-sided large objects," *Inverse Prob. Sci. Eng.* **25**(11), 1676–1696 (2017).
15. M. K. Nguyen and T. T. Truong, "Inversion of a new circular-arc Radon transform for Compton scattering tomography," *Inverse Prob.* **26**(6), 065005 (2010).
16. G. Rigaud, M. K. Nguyen, and A. K. Louis, "Novel numerical inversions of two circular-arc radon transforms in Compton scattering tomography," *Inverse Prob. Sci. Eng.* **20**(6), 809–839 (2012).
17. C. Tarpau and M. K. Nguyen, "A novel modality of Compton scattering tomography, image formation and reconstruction," in *Proc. Int. Conf. Image Process. Comput. Vision, and Pattern Recognit. (IPCV'19)*, Las Vegas, pp. 60–65 (2018).
18. J. Cebeiro et al., "An interior Compton scatter tomography," in *IEEE Nucl. Sci. Symp. and Med. Imaging Conf. 2018 (IEEE NSS/MIC'18)*, Sydney, Australia (2018).
19. C. Tarpau and M. K. Nguyen, "Scattering imaging system with dual configurations," *Proc. SPIE* **11172**, 111720Y (2019).

20. C. Tarpau et al., "A new concept of Compton scattering tomography and the development of the corresponding circular Radon transform," *IEEE Trans. Radiat. Plasma Med. Sci.* 1–1 (2019).
21. T. T. Truong and M. K. Nguyen, "New properties of the V-line Radon transform and their imaging applications," *J. Phys. A: Math. Theor.* **48**(40), 405204 (2015).
22. R. N. Bracewell, "Numerical transforms," *Science* **248**(II May), 697–704 (1990).
23. J.-C. Nosmas, "Analyse Microlocale et Tomographie Géométrique," in *ICAOS'96*, Springer, pp. 338–344 (1996).
24. V. P. Krishnan and E. T. Quinto, "Microlocal analysis in tomography," in *Handbook of Mathematical Methods in Imaging*, O. Scherzer, Ed., pp. 1–50, Springer, New York (2014).
25. J. Frikel and E. T. Quinto, "Artifacts in incomplete data tomography with applications to photoacoustic tomography and sonar," *SIAM J. Appl. Math.* **75**(2), 703–725 (2015).
26. E. T. Quinto, "Artifacts and visible singularities in limited data x-ray tomography," *Sens. Imaging* **18**(1), 9 (2017).
27. O. A. O. Guerrero et al., "Attenuation correction in a new modality of Compton scattering tomography," in *Interdiscip. Symp. Signal and Syst. for Med. Appl. (ISSSMA)*, Paris, France (2013).
28. C. Tarpau, J. Cebeiro, and M. K. Nguyen, "A new bi-imaging NDT system for simultaneous recovery of attenuation and electronic density maps," in *Eleventh Int. Conf. Non Destruct. Test. Aerosp.* (2019).
29. J. W. Webber and W. R. Lionheart, "Three dimensional Compton scattering tomography," *Inverse Prob.* **34**(8), 084001 (2018).
30. J. W. Webber and S. Holman, "Microlocal analysis of a spindle transform," *AIMS Inverse Prob. Imaging* **13**(2), 231–261 (2019).

Cécilia Tarpau has been a PhD candidate at the Science and Information Technology and Communication since October 2018 under the direction of Mai K. Nguyen, Laurent Dumas, and Geneviève Rollet. Her doctoral research investigates new Compton scattering tomography modalities and their associated Radon transforms. Her thesis title is "Concept and modeling of new Compton scattering tomography modalities."

Mai K. Nguyen received her PhD in signal and image processing from Grenoble National Polytechnic Institute, France, in 1988. She has been a professor in the Department of Computer Science at the University of Cergy-Pontoise since 2005. Her research interests include inverse problems, generalized Radon transforms, and their applications in imaging science, scattered ionizing radiation imaging, biomedical imaging, and nondestructive evaluation. She is an IEEE senior member.